SANDIA REPORT
SAND2024-13308R
Printed September 2024

Sandia National Laboratories

A hybrid-kinetic simulation tool for non-thermal warm x-ray z-pinch sources, with gas-puff and wire array exemplars

Nichelle Bennett

Prepared by
Sandia National Laboratories
Albuquerque, New Mexico 87185
Livermore, California 94550

Issued by Sandia National Laboratories, operated for the United States Department of Energy by National Technology & Engineering Solutions of Sandia, LLC.

Available to DOE and DOE contractors from

U.S. Department of Energy
Office of Scientific and Technical Information
P.O. Box 62
Oak Ridge, TN 37831

Telephone: (865) 576-8401
Facsimile: (865) 576-5728
E-Mail: reports@osti.gov
Online ordering: http://www.osti.gov/scitech

Available to the public from

U.S. Department of Commerce
National Technical Information Service
5301 Shawnee Road
Alexandria, VA 22312

Telephone: (800) 553-6847
Facsimile: (703) 605-6900
E-Mail: orders@ntis.gov
Online order: https://classic.ntis.gov/help/order-methods

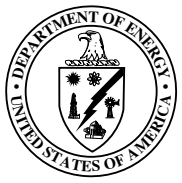

ABSTRACT

Increasing the fluence of z-pinch x-ray radiation sources above ~ 10 keV has been a long-standing goal for scientists at Sandia National Laboratories' Z Machine. Optimizing sources for non-thermal "cold Kα" emission in higher atomic-number materials appears to be a promising path to increase warm x-ray yield [Ampleford, *et al.*, SAND2015-10453]. However, this emission is generated by supra-thermal electrons, which are not treated in the magnetohydrodynamic (MHD) codes that are typically used in z-pinch source development. MHD codes do not allow for charge separation or space-charge-generated electric fields, and constrain particle kinematics to Maxwellian distributions. The kinetic codes which do accommodate discrete, non-thermal energy distributions are computationally prohibitive when modeling plasmas near solid density and when modeling/tracking higher ionization states. Thus, modeling non-thermal z-pinch sources requires a new simulation tool.

In this report, we present a new hybrid modeling capability that uses the fast features of MHD-type particles to the greatest extent possible, then transitions to the slower but more complete kinetic particle treatment to correctly capture the particle energy spectra that generate non-thermal emission. This capability is founded on the fully-relativistic particle-in-cell code CHICAGO, which already includes fluid particle treatments [Welch, *et al.*, Phys. Plasmas 16, 123102 (2009)]. The governing equations and hybrid methodology presented here are applied in simulations of an argon gas-puff and a molybdenum wire-array to provide preliminary code validation.

The argon simulation is compared to measured implosion times and yields from Jones *et al.*, Phys. Plasmas **22**, 020706 (2015). The simulated x-ray yield is within 25% of measurements and the implosion times agree within a few percent. The molybdenum wire array simulation captures the implosion timing reported in Hansen *et al.*, Phys. Plasmas **21**, 031202 (2014), but work is needed to verify the available EOS table. These exemplar simulations represents the type of non-thermal sources that will be developed using the hybrid code capability going forward.

This page intentionally left blank.

ACKNOWLEDGMENT

The author wishes to thank Christopher Jennings for providing the 2D density distributions for the Ar gas puff and Kyle Cochrane for providing IDL routines to convert sesame EOS tables into the Propaceous format. Thank you, too, to Mark Hess, who contributed to the wire-array simulations and yield estimates, but whose work is not included in this report. The results presented were ultimately made possible by the code upgrades provided by Eric Watson and Dale Welch of Voss Scientific, LLC. which removed bugs and significantly reduced run times.

This page intentionally left blank.

CONTENTS

This page intentionally left blank.

LIST OF FIGURES

This page intentionally left blank.

NOMENCLATURE

EOS equation of state

LTE local thermal equilibrium

MHD magneto-hydrodynamics

PIC particle-in-cell

QN quasi-neutral

Z atomic number

$\bar{Z}$ ionization state

This page intentionally left blank.

1. INTRODUCTION

Increasing the fluence of z-pinch x-ray radiation sources above ~ 10 keV has been a long-standing goal for scientists at Sandia National Laboratories' Z Machine. In general, z-pinch radiation sources are thermal with efficient photon emission in the energy range at or below the plasma temperature (~ 2.5 keV for the Z Machine, [2]). The output spectrum is varied through the choice of plasma species. To create a warm x-ray source, a low to mid-atomic number (Z) element implosion generates non-Planckian radiation dominated by K-shell and L-shell transitions. High-yield line-transition sources on the Z Machine include aluminum wire arrays, with peak yields of 375 kJ in the $h\nu \sim 1 - 2.5$ keV range, and Ar gas puffs, with peak yields of ~ 350 kJ near 3.3 keV [14, 20, 13, 2, 1, 21, 24].

As the atomic number of the plasma species increases, the plasma temperature falls below the K-shell transition energy, limiting the yield. Examples of higher-Z elements fielded on the Z Machine include Kr gas puffs with $h\nu \sim 13$ keV and Mo wire arrays with $h\nu \sim 17$ keV and kJ-scale yield [17]. Although the published yields in this energy range are low (above 15 keV, yields are less than 10 kJ [12]), they can be higher than expected from the magneto-hydrodynamic (MHD) simulations used in source development. This is because the higher-Z sources have non-thermal K-shell emission, while MHD predicts only thermal output. Optimizing x-ray sources for non-thermal emission to increase fluence above 10 keV, but requires a new simulation tool.

In this report, we describe a new code capability that is better suited to predict and optimize non-thermal yield. Studies on the Z Machine have shown that non-thermal sources have similar implosion characteristics but different pinch stagnation profiles from thermal sources [1]. To capture both stages as accurately as possible, a hybrid particle treatment has been implemented in the fully-relativistic electromagnetic particle-in-cell (PIC) code CHICAGO. The ionization and implosion stages are modeled with a fast, quasi-neutral (QN) particle treatment, similar to an MHD fluid in which electrons are not tracked but assumed to follow the ions. This includes the assumption of local thermal equilibrium (LTE) with an equation-of-state (EOS) and radiation transport. Prior to stagnation, the particles are transitioned to fully-kinetic electrons and ions. Tracking electrons requires high spatial, temporal, and charge resolution, as demonstrated in Ref. [7], but provides the more accurate, discrete particle energy distributions that drive non-thermal processes. The field and particle space-charge dynamics are calculated self-consistently. At present, the non-LTE spectral features are calculated in a post-processing step. While the thermal, LTE spectrum is modeled in the QN phase, a self-contained calculation of the non-thermal particle generation and output photon spectrum requires considerable further development.

Although the hybrid-kinetic PIC approach is computationally expensive, it is required to simulate the supra-thermal particles generating non-thermal yield. The non-thermal process is being pursued because it has the potential to scale favorably with current, as discussed briefly in Sec. 2. (This section is largely reproduced from Ref. [3].) The hybrid PIC code specifications and new modifications are detailed in Sec. 3. The fluid and kinetic particle treatments are reviewed in Sec. 3.1 and the transitions techniques between these treatments are described in Sec. 3.2. The resolution constraints on the hybrid treatment are discussed in the demonstration of the technique in Sec. 3.2.

The code is tested using an Ar gas puff, to determine its suitability for modeling z-pinch sources. The 1D and 2D simulations are described in Sec. 5. Initially, an idealized 1D model is used to determine the required spatial and temporal resolution for modeling non-transitioning QN, multi-fluid, and kinetic particles. This is described in Sec. 5.1. While the Ar gas puff is a thermal source, the kinetic dynamics show a broader sheath than might be predicted in MHD. A high-resolution 2D simulation of an Ar gas puff [18] demonstrates the full code capability in Sec. 5.2, including the hybrid particle treatment and transitions.

Finally, a non-thermal Mo wire array is modeled in 2D. Such wire-array simulations are not commonly conducted for the Z Machine, even in MHD. The results are presented in Sec. 6. The Mo wire array represents the type of non-thermal source simulation that will utilize the hybrid code capability going forward.

2. K-SHELL TRANSITIONS AS A PROMISING PATH TO HIGHER WARM X-RAY YIELDS

The Ar gas puffs and Al, stainless steel, and Cu wire arrays operate as K-shell Heα and Lyα emitters. The radiation from these thermal sources can be understood using the graphic in Fig. 2-1a, which is reproduced, along with most of this discussion, from Ref. [3]. A target constructed of lower Z material becomes highly ionized during the pinch, such that the outer, lower-energy electron orbits are not fully populated. An x-ray is emitted as a bound electron transitions into the K shell or L shell.

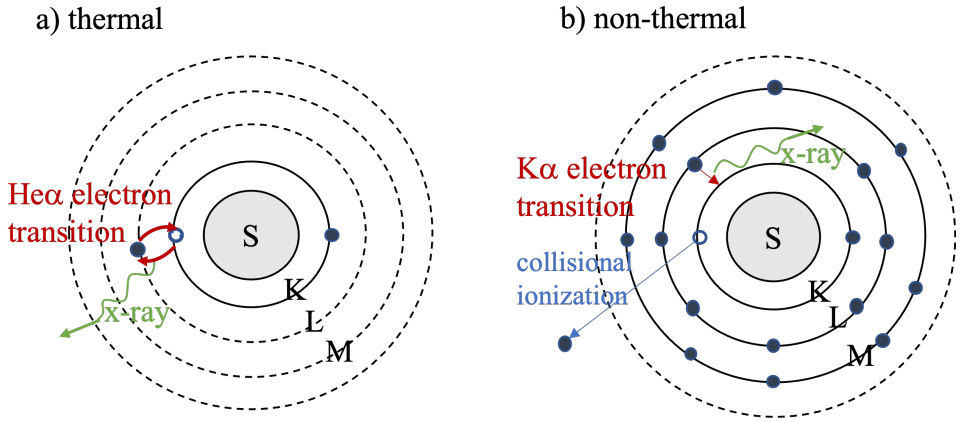

Figure 2-1 Illustrations of the orbital transitions that create a) thermal Heα x-rays and b) non-thermal "cold" Kα x-rays. This graphic is modified from the original appearing in Ref. [3].

In the non-thermal process, illustrated in Fig. 2-1b, a higher-Z material is weakly ionized, retaining most of its inner shell electrons. A collision with a supra-thermal particle (typically a free electron) strips a bound electron from the 1s orbital state, which is subsequently filled by an electron from the 2p state. This is referred to as "cold Kα" emission.

Cold Kα emission suffers less radiative losses from heating and ionization than thermal emission. It also scales more favorably with photon energy, as shown in Fig. 2-3, which is reproduced from Ref. [3]. Figure 2-3 shows the measured yields from thermal K-shell emission decreasing logarithmically with the ion transition energy [12], and indicating a material-independent peak (Maxwellian) plasma temperature of 2.5 keV at stagnation. (Figure 2-3 does not include the results from advanced sources on Z with x-ray yields above 10 keV [15, 30].) In contrast, the cold Kα yield is a flatter function of energy and has an apparent 60-keV temperature.

Figure 2-3 suggests the possibility of extending the spectral range of z-pinch x-ray sources by optimizing cold-Kα production. While modeling a source constructed of a high-Z material is within the scope of our MHD codes, optimizing it for cold-Kα yield is beyond the scope. This required the development of a hybrid kinetic code that can model a plasma with thermal and supra-thermal particles, which is described in the next section. The full particle kinetics are included, but the ability to generate the non-LTE spectra in Fig. 2-2 requires further development.

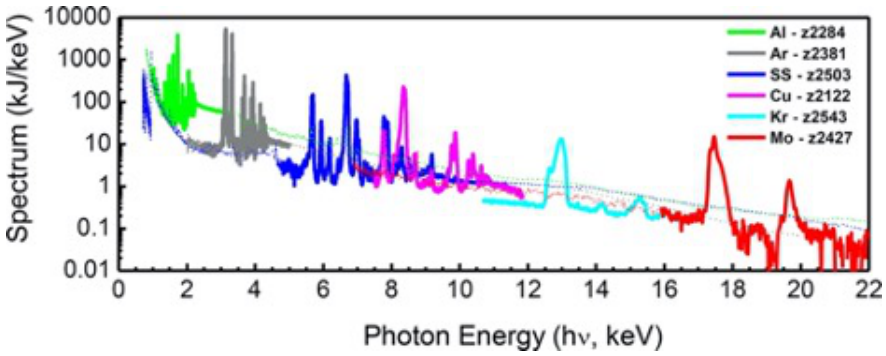

Figure 2-2 The yields from various warm x-ray source materials versus energy from Ref. [1]. The yield is binned in kJ/keV.(Figure reproduced from Ref. [3].)

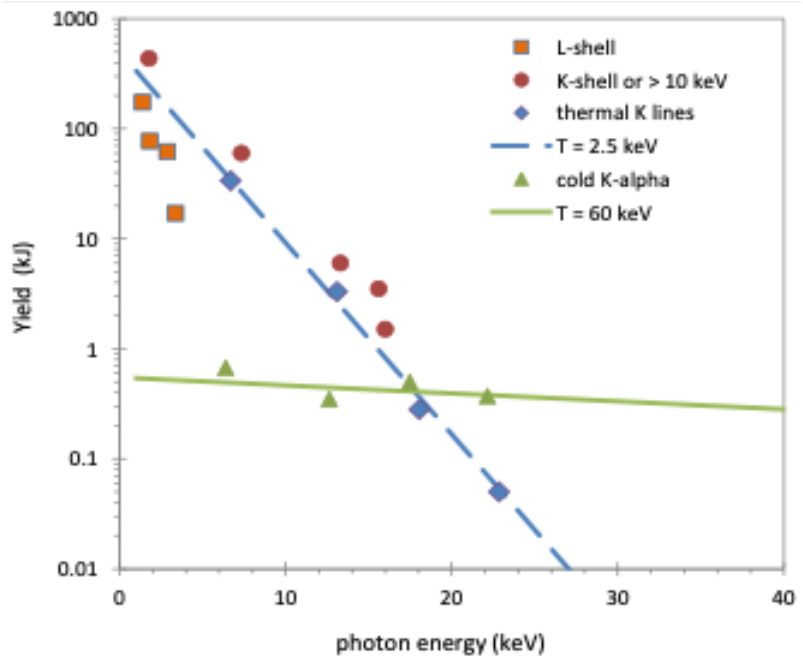

Figure 2-3 Warm x-ray yields as a function of photon energy from thermal (blue) and non-thermal (green) sources on Z. (Figure reproduced from Ref. [3].)

3. KINETIC MODEL DEVELOPMENT

A kinetic code is required for optimizing non-thermal x-ray sources for four reasons:

1. Particles are tracked discretely. Particle momenta are recorded individually, giving rise to non-Maxwellian energy distributions.
2. A PIC code pushes particles through a grid which allows for species interpenetration and non-thermal conditions.
3. Charge neutrality is not enforced. Space-charge distributions form when modeling particles kinetically. This both generates and is a consequence of discrete energy distributions and particle interpenetration (high momentum and long mean free paths).
4. The full set of Maxwell's equations is used, including Gauss' Law and the displacement current.

The first item enables the non-Maxwellian particle distributions which define non-thermal radiation [17]. By contrast, the MHD fluid is an assemblage that assumes thermalization and, typically, Maxwellian energy distributions. The second item gives rise to the third: species interpenetration may generate space-charge distributions. These impact the fourth item because they generate currents and fields that don't exist in MHD.

The equations governing the kinetic model are detailed in Sec. 3.1. The electromagnetic PIC code CHICAGO is used here because it enabled us to build on existing particle treatments [26, 34], described in Secs. 3.1 and 3.2. The particle and field advances are interleaved (the "leap-frog" method), which necessitates resolution constraints. The benefit is a self-consistent particle and field advance in which the fields accelerate the charged particles that then impact the field calculations.

3.1. Particle equations of motion in the hybrid PIC code CHICAGO

The fundamental equations governing particle and field propagation are the Lorentz force on an individual particle and Maxwell's equations:

$$
\begin{aligned}
m_\alpha \frac{d(\gamma_\alpha \mathbf{v}_\alpha)}{dt} &= q_\alpha(\mathbf{E} + \mathbf{v}_\alpha \times \mathbf{B}) - \nu_{\alpha\beta} m_\alpha (\mathbf{v}_\alpha - \mathbf{v}_\beta) && (1)\\
\epsilon\mu \frac{\partial \mathbf{E}}{\partial t} &= \nabla \times \mathbf{B} - \mu \mathbf{j} && (2)\\
\frac{\partial \mathbf{B}}{\partial t} &= -\nabla \times \mathbf{E} && (3)\\
\nabla \cdot \mathbf{E} &= \frac{\rho_e}{\epsilon} && (4)\\
\nabla \cdot \mathbf{B} &= 0.
\end{aligned}
$$

PIC codes typically solve Eqs. 2 through 4 for the fields. Eq. 1 is the equation of motion for kinetic particles, where ν_{ij} is the collision frequency. This collision term may be replaced by a

binary collision model. The Coulomb collision frequency is supplied by Spitzer for species α scattering off species β [23]:

$$\nu_{\alpha\beta} = \frac{4\sqrt{2\pi}e^4 Z_\alpha^2 Z_\beta^2 n_\beta \ln\Lambda_{\alpha\beta}}{(4\pi\epsilon_0)^2\, 3 m_\alpha m_{\alpha\beta}} \left(\frac{T_\alpha}{m_\alpha} + \frac{T_\beta}{m_\beta}\right)^{-3/2}, \tag{5}$$

where $m_{\alpha\beta} = m_\alpha m_\beta/(m_\alpha + m_\beta)$ and $\ln\Lambda_{\alpha\beta}$ is the Coulomb logarithm.

In the kinetic treatment, the electron cyclotron frequency (ω_{ce}) and plasma frequency (ω_{pe}) must be resolved to some level to capture the collisions and orbits generated by Eq. 1. The required ω_{ce} and ω_{pe} resolution are determined by the specific implicit technique used in the particle push. The value of $\omega_{ce}\Delta t = 1.5$ that is used in simulations in this report is enabled by the Magnetic Implicit solution in Chicago [16, 31]. Still, high combined spatial and charge resolution is required in the kinetic simulations due to the artificial collisionality inherent in an energy-conserving algorithm. This artificial collisionality is reduced by a cloud-in-cell treatment [9, 33].

In a companion study, we report that energy and momentum conservation require a grid resolution that may be defined in units of electron collisionless skin depth, $l_s = c/\omega_p$ [7]. Using a criterion for conserving energy of $\Delta E/E_{tot} < 0.01$ for 50,000 time steps, a linear cloud distribution requires a *very approximate* grid resolution of $\Delta x = 3l_s$ for densities $10^{15} - 10^{20}$ cm^{-3}. For a second-order cloud distribution the criterion is $\Delta E/E_{tot} < 0.005$ yielding $\Delta x \leq 15 l_s$. Thus, the second-order is the more stable cloud-in-cell distribution. Note, these scalings are functions of a set of v_d, Δt, particles-per-cell, and number of steps.

In addition to the kinetic particle treatment typical of PIC codes, Chicago includes fluid treatments for particles, modifying Eq. 1 (with particle energy equations) while retaining Eqs. 2 through 4. This is possible because particles are separate entities from the grid cells. The multi-fluid treatment, or inertial fluid, available in Chicago is the most similar to kinetic and has the same spatial resolution requirements. This is because the equation of motion for inertial fluids is identical to kinetic with the addition of the pressure term which describes intra-species collisions [32]. The standard collision term is retained for inter-species scattering. The equations of motion for electron and ion species, without the thermal force, are [34, 27, 32]

$$\begin{aligned} m_e\frac{d\mathbf{v}_e}{dt} &= -e\left(\mathbf{E} + \frac{\mathbf{v}_e}{c}\times\mathbf{B}\right) - \frac{\nabla p_e}{n_e} - m_e\nu_{ei}(\mathbf{v}_e - \mathbf{v}_i), \\ m_i\frac{d\mathbf{v}_i}{dt} &= e\bar{Z}\left(\mathbf{E} + \frac{\mathbf{v}_i}{c}\times\mathbf{B}\right) - \frac{\nabla p_i}{n_i} - m_i\nu_{ij}(\mathbf{v}_i - \mathbf{v}_j), \end{aligned} \tag{6}$$

The inertial fluid model avoids numerical cooling by including a separate equation for particle energy. The electron and ion internal energies advance using [26, 32]

$$\begin{aligned} \frac{dU_\alpha}{dt} &= -\frac{p_e\nabla\cdot\mathbf{v}_\alpha}{n_\alpha} + \frac{\nabla\cdot(\kappa_e\nabla T_\alpha)}{n_\alpha} + \sum_\beta \nu_{\alpha\beta}\frac{m_\alpha m_\beta}{m_\alpha + m_\beta}(\mathbf{v}_\beta - \mathbf{v}_\alpha)^2 \\ &\quad + \sum_\beta \frac{3m_\alpha\nu_{\alpha\beta}}{m_\alpha + m_\beta}(T_\beta - T_\alpha) + \dot{E}_{rad}. \end{aligned} \tag{7}$$

The last term accounts for emission/absorption of radiation when an EOS treatment is used. Viscosity terms may be added to Eq. 6 and Ref. [27] suggests this is useful to avoid numerical problems at shock fronts. The viscosity tensor is part of the suite of classical transport coefficients along with electrical conductivity, thermal conductivity, and thermoelectric coefficients [11, 4, 10]. It is represented as [10]

$$\Pi^{\alpha}_{kl} = -\mu^{\alpha}_{klmn}\nu_{mn} \tag{8}$$

where Π^{α} is the pressure tensor for species α, μ^{α}_{klmn} is the viscosity tensor for species α, and

$$\nu_{mn} = \frac{\partial v_n}{\partial x_m} + \frac{\partial v_m}{\partial x_n} - \frac{2}{3}\delta_{mn}\nabla \cdot \mathbf{v}.$$

The maximum values for the viscosity coefficients are determined by the simulation spatial and temporal resolution. For electrons, $\mu^{e}_{max} = 0.5\Delta x^2/\Delta t$, and for ions, $\mu^{i}_{max} = (m_i/m_e)\mu^{e}_{max}$.

While the kinetic treatment is the most realistic, multi-fluid particles have the advantage of faster simulation run times for a few reasons. First, collisions within a species are not modeled but are assumed to obey a Maxwell distribution. This, in turn, enables the number of particles, or charge resolution, to be reduced, particularly when the Eulerian remap is used. Third, an EOS treatment is available for multi-fluid in which the electron and ion charge-to-mass is adjusted based on $\bar{Z}$. This replaces the costly Monte Carlo PIC ionization method.

The QN treatment [27, 28] is the fastest of the three and enjoys a lower resolution requirement because electron inertia is neglected. In the QN model, the assumption is $\rho_e \sim 0$ or, equivalently,

$$n_e = \sum_{k=1}^{N_i} \bar{Z} n_k,$$

where Z_k is the charge state of the kth ion. Therefore, it is possible to follow an ion macroparticle which carries the fluid information for the inertia-less electrons (which have no equation of motion). This treatment most closely resembles MHD. The equation of motion for the composite ion-electron macroparticle is [27]

$$m_i n_i \frac{d\mathbf{v}}{dt} = \mathbf{j} \times \mathbf{B} - \nabla(p_e + p_i), \tag{9}$$

where p_e is the electron pressure. When multiple quasi-neutral ion species are modeled, the current becomes [27]

$$\mathbf{j} = \sigma \left[\mathbf{E} + \mathbf{v}_+ \times \mathbf{B} - \frac{1}{e n_e}\left(\nabla p_e + \beta \nabla T_e\right) - \frac{m_e}{e}\sum_{k=1}^{N_i} \nu_{ek}(\mathbf{v}_k - \mathbf{v}_+) \right]$$

where

$$\mathbf{v}_+ = \sum_{k=1}^{N_i} \rho_k \mathbf{v}_k$$

and

$$\rho_k = \frac{\bar{Z} n_k}{n_e}.$$

The current is substituted for the electric field such that the MHD multi-ion momentum equations are

$$\begin{aligned} m_i n_i \frac{d\mathbf{v}_k}{dt} &= \rho_k \mathbf{j} \times \mathbf{B} - \nabla p_k - \rho_k \nabla p_e + \rho_k \beta n_e \nabla T_e \\ &\quad -n_k m_k \sum_{k=1}^{N_i} \nu_{kl}(\mathbf{v}_k - \mathbf{v}_l) \\ &\quad -n_e m_e \nu_{ek}(\mathbf{v}_k - \mathbf{v}_+) + e n_e \rho_k \nu_{ek}(\mathbf{v}_k - \mathbf{v}_+) \times \mathbf{B} \\ &\quad +\rho_k n_e m_e \sum_{k=1}^{N_i} \nu_{el}(\mathbf{v}_l - \mathbf{v}_+) + \frac{m_e}{e}(\rho_k \nu_e - \nu_{ek})\mathbf{j} \end{aligned} \tag{10}$$

The fields, currents, densities, and electron pressure gradient are all calculated at the nodes and then interpolated to the macroparticle position when Eq. 9 is applied.

3.2. Hybrid PIC technique

There are two particle migration models available in CHICAGO to transition between the particle equations of motion. One is a transition of individual particles as they exceed a directed or thermal energy threshold [34, 8] and the other is an *en masse* transition for all particles from one treatment to another [5]. The recent code developments described here have made these transition techniques more generic and robust. We note that the studies presented here, as well as the resolution study in Ref. [7], use the same implicit field and particle solutions as in recent power-flow publications using CHICAGO [32, 6].

The *en masse* migration now accommodates transitions to multiple ion species based on a specified fractional split, and the recipient species may be kinetic or multi-fluid. The algorithm identifies the appropriate ion/electron pairs as recipient species based on the ion's equation of motion.

The EOS algorithm was modified to enable a single table to describe multiple ion species. This is solely for defining a single physical ion as both multi-fluid and quasi-neutral. Maintaining charge conservation is more difficult in the multi-fluid treatment as ions change $\bar{Z}$ and this charge must be scattered to surrounding electrons. The Eulerian remap mitigates this problem by essentially creating a more matched pair of electron and ion macroparticles. The electrons associated with the two ion equations of motion have been deconflicted.

The individual transition technique may not conserve charge when using an EOS. Because electrons and ions are distinct in the multi-fluid treatment, migrating particles will also be distinct. This leaves the likely scenario in which a fluid electron macroparticle is converted to kinetic, but the ion is not. The EOS then compensates the ion $\bar{Z}$ with additional fluid-electron charge. The converse may also occur. The multi-fluid transition is not used for non-thermal source development for this reason.

4. HYBRID PARTICLE MIGRATION TECHNIQUE SUITABLE FOR z-PINCHES

We explored the option of a multi-tiered QN-to-kinetic migration in which the simulation is initialized as QN then migrated in bulk to a multi-fluid treatments before engaging individual particle transitions to kinetic. This method is not useful for a gas puff or wire array model, or any of the z-pinches explored in this study. The primary reason is stated in Sec. 3.2 above, namely, the likelihood that charge will not be conserved in a multi-fluid transition to kinetic. The secondary reason is the resolution requirements for multi-fluid are the same as for kinetic while a multi-fluid plasma sheath tends to compress into a single grid cell. For the gas puff and wire array simulations presented here, the multi-fluid simulations demonstrated no saving in compute resources or run times.

We also explored the benefits of a various transition criterion to automate the decision to migrate from QN to kinetic. The collision frequency (ν_{ij} or ν_c) and the Hall parameter ($\omega_{ce}\nu_c$) were shown to be equally discriminating, as plotted in Fig. 4-1. The sheath maintains values of ν_c and $\omega_{ce}\nu_c$ that differ from the interior plasma by at least four orders of magnitude for the duration of the implosion. What this also suggests, as discussed in Sec. 5.1, is that there are also kinetic effects impacting the sheath for the duration of the pulse. However, these do not significantly impact the implosion time or yield.

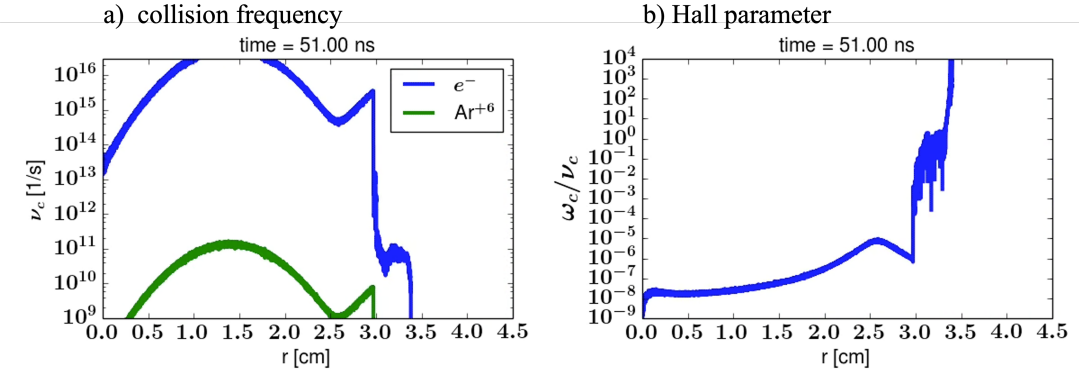

Figure 4-1 The a) collision frequency and b) Hall parameter early in the pulse in a 1D gas puff simulation.

A previous report investigated the maximum allowable $\omega_{ce}\Delta t$, the most stable cloud-in-cell function, and the resolution required for a power-flow plasma up to 10^{20} cm^{-3} in density [7]. We have more recently investigated the impact of fluid streaming parameters in load modeling and the resolution required for wire arrays and advanced x-ray sources. We found the MHD-type parameters such as viscosity and streaming factors were best minimized and that the resolution results in Ref. [7] hold for load models, and may even by exceeded by up to an order of magnitude.

The hybrid technique for modeling near-solid-density loads is to initialize the simulation using QN particles with an EOS and opacity tables for each ion species. The ionization states are

updated for each individual macroparticle and do not require separate species for each ionization state. The ionization and implosion stages are modeled with QN particles and radiation transport. Just prior to implosion, the particles transition *en masse* to kinetic, freezing the ionization state for each particle. (This is distinct from kinetic breakdown or ionization models in which each charge state requires a separate particle species.) For our load simulations, we use

- a Courant multiplier of 3.0 for QN,
- $\omega_{ce}\Delta t = 2$ for kinetic,
- MHD streaming factor < 0.002,
- MHD vacuum electron density = 10^{13} cm^{-3},
- MHD vacuum collision frequency = 10^{12} cm^{-3},
- second order cloud-in-cell weighting for kinetic.

An Eulerian remap is used for the QN particles. Transitioning to kinetic is then a conversion from a single particle per cell to may ion and electron macroparticles per cell. Increasing the number of kinetic particles improves charge neutrality, and more kinetic particles are required when transitioning to higher Z materials at high ionization states. For Ar (in 1D), we found as few as 20-50 particles per cell may be sufficient with 5 μm grid resolution. During the transition, charge conservation is enforced in Chicago, as shown in Fig. 4-2a. Figure 4-2b shows that energy is nearly conserved. The discrepancy is due to the time centering of the Magnetic Implicit push and the energy calculation. This error does not occur when the explicit solver is used, but Magnetic Implicit being essential to z-pinch simulations, the time-centering in the history output is being corrected.

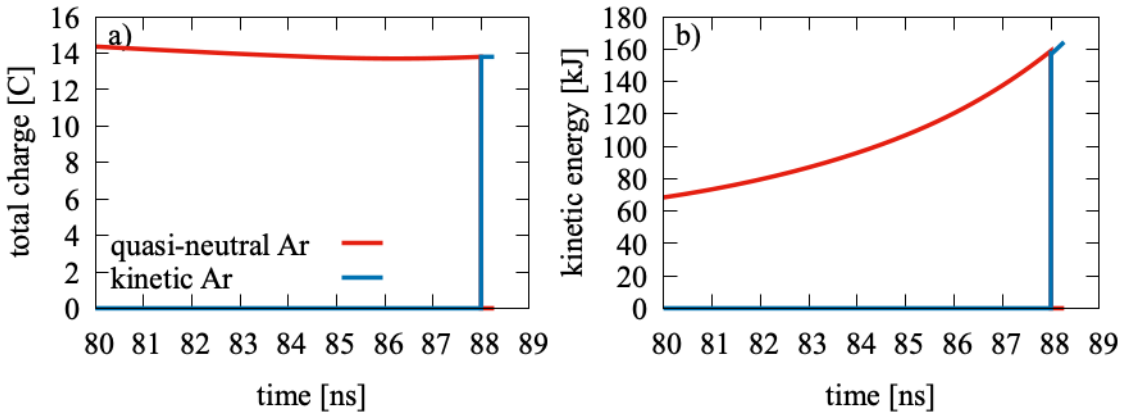

Figure 4-2 The summed Ar ion a) charge and b) kinetic energy in a 1D gas puff simulation with a QN to kinetic migration at 88 ns.

5. GAS PUFF DYNAMICS

The new hybrid technique is tested using 1D and 2D Ar gas puff simulations. The 1D models use idealized voltage pulses and Gaussian density profiles to test spatial and temporal resolution requirements. The kinetic and QN models are compared in Sec. 5.1. The kinetic models show more radial penetration and higher particle velocities during implosion than seen in a QN or MHD model.

The 2D model uses a realistic Z voltage pulse to drive a more realistic initial gas-puff density distribution (see Ref. [21]). The stagnation conditions achieved are similar to the measurements presented in Ref. [19].

5.1. 1D Ar gas puff models

Kinetic 1D simulations, with $\bar{Z}$ initialized to 1, 2, and 6, provide the most realistic particle transport, with complex the energy and spatial distributions, for interpenetrating electrons and ions. Convergence studies demonstrate the spatial resolution must increase with the electron population, as defined by the initialized $\bar{Z}$. Further study is needed to determine the ideal resolution during the pinch, which likely varies by the z-pinch stagnation conditions.

The 1D simulations use a simple linear pulse rise, which is unrealistically fast. The peak current of 15.5 MA is reached in 69 ns. The differences in a QN and kinetic treatment become obvious during the initial implosion. The kinetic simulation with Ar^{+6} is compared to a QN fluid in which the electron population is determined by the EOS $\bar{Z}$. The plasma densities for both cases are compared in Fig. 5-1. The kinetic sheaths are wider, and not impacted by increased grid resolution, while the QN sheaths and, in particular, the multi-fluid sheaths, tend to span one to a few cells, even when those cells shrink.

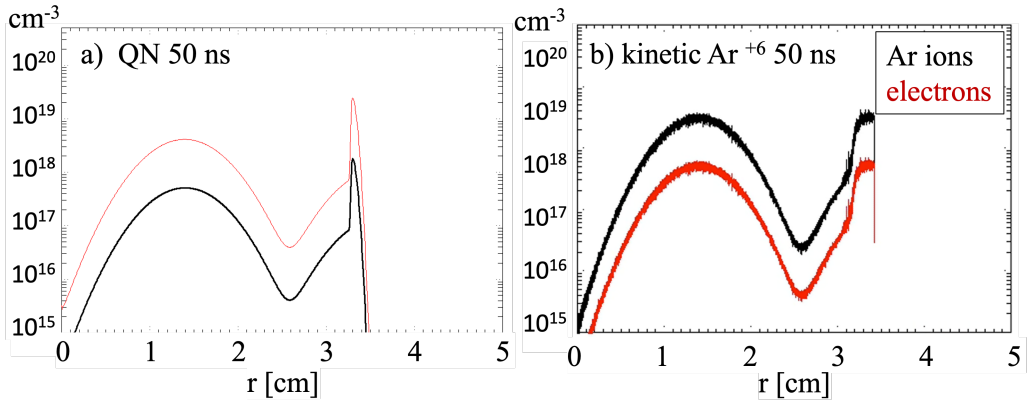

Figure 5-1 The imploding plasma sheaths in 1D a) QN and b) kinetic Ar^{+6} gas puffs.

We determined that there are no benefits to using multi-fluid particles in a load model. The multi-fluid particles had the idealized sheath behavior of a QN particle with the resolution requirements of kinetic electrons. The result was an ever-tightening sheath, with increasing

number density. This required ever-smaller time steps to comply with limits on $\omega_{ce}\Delta t$ and $\omega_p \Delta t$.

The electron kinetics are interesting for this 1D test. Plots of electron kinetic energy, in units of $\gamma - 1$ are shown in Fig. 5-2 for three times during the implosion. In a kinetic model, the underlying physics of the $\mathbf{j} \times \mathbf{B}$ motion of the sheath is the $\mathbf{v} \times \mathbf{B}$ motion of individual particles. This generates different acceleration for the discretized velocities. While the accelerating force increases with the pulse rise, some electrons have already penetrated the cooler, non-imploding plasma. This gives rise to the energy-radial profiles in Fig. 5-2. Lastly, the non-Maxwellian energy distributions of the kinetic electrons (for the Ar^{+6} case) are plotted in Fig. 5-3.

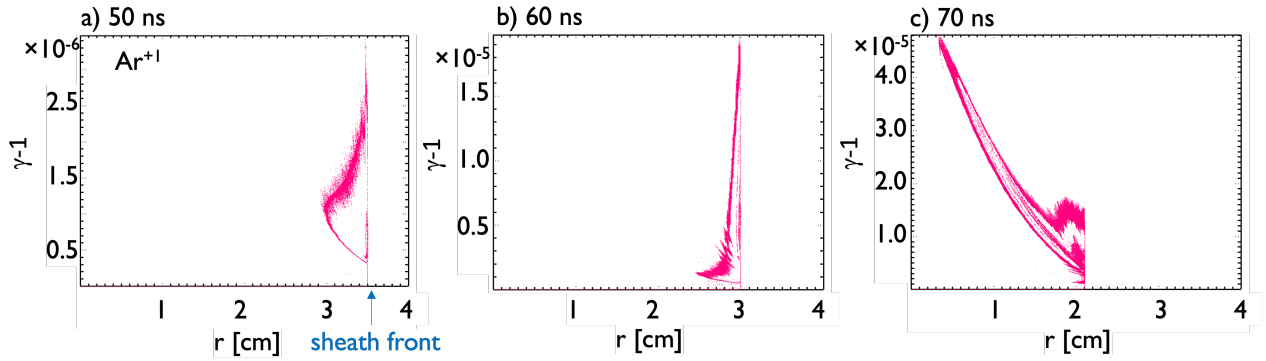

Figure 5-2 The electron $\gamma - 1$ versus radius in a kinetic 1D Ar^{+1} puff.

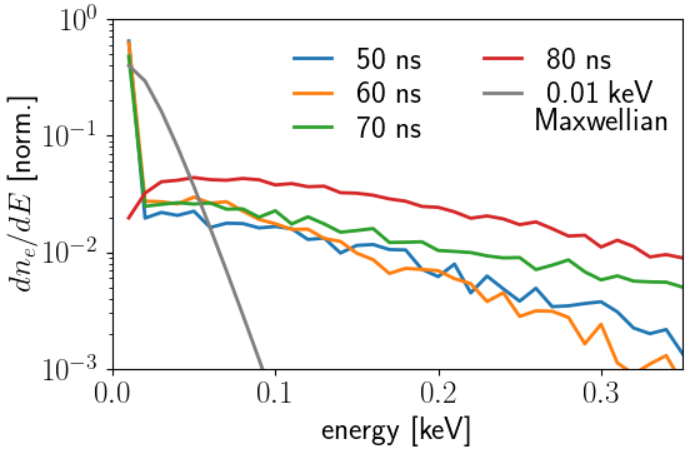

Figure 5-3 The electron energy distributions in a kinetic 1D Ar^{+6} puff.

5.2. 2D Ar gas puff model

The 2D Ar gas puff model uses the resolution results from the 1D tests. Here, the simulation is driven by an actual Z pulse and the initial distribution of gas density is more realistic, taken from the two-jet configuration published in Ref. [21]. The initial Ar density distribution is plotted in Fig. 5-4a.

Two versions of the simulation are performed, one using the hybrid technique outlined in Sec. 4 and a second continuing with the QN model without transition. The latter is used to estimate the yield generated in the radiation transport algorithms.

For the QN-only model, the density redistribution through implosion is shown in Figs. 5-4b through f. A resolution of 10 μm is needed to reduce spurious implosion features caused by grid stair-stepping. It is not clear if the plasma behavior at the interface with the perfectly conducting boundaries is realistic. The current penetrates the sheath somewhat at the axial extents causing a trailing plasma.

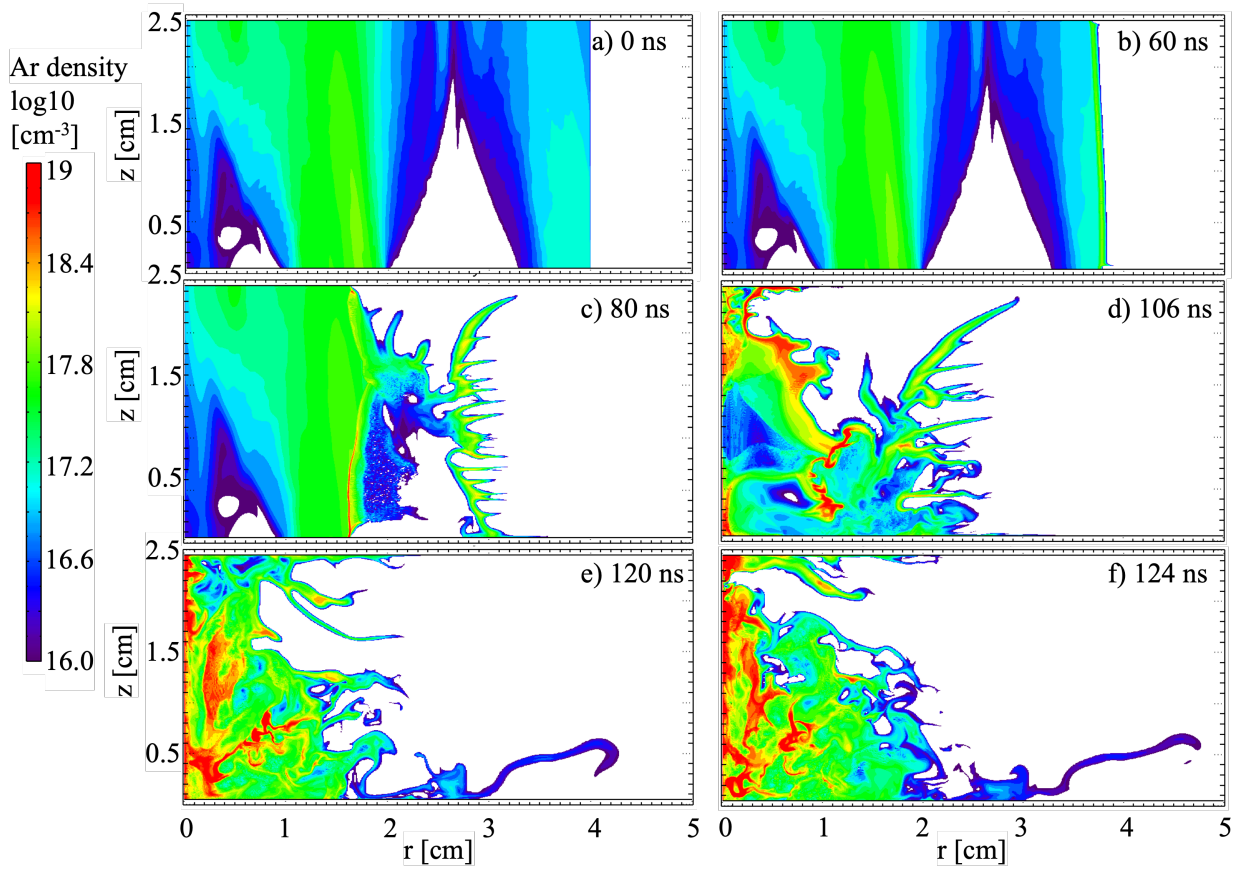

Figure 5-4 The Ar gas-puff implosion in a 2D QN simulation. The Ar density distributions are shown at six times: a) 0, b) 60, c) 80, d) 106, e) 120, and f) 124 ns.

This low density is unlikely to be resolved by a plasma imaging diagnostic, such as shown in Ref. [19], but the proportion of trailing plasma is very roughly consistent with measurement. The

measured results from Ref. [19] are described as:

> The model that best fits the data consists of a hot core ($T_e = 2.45$ keV, $n_i = 6.7 \times 10^{19}$ cm^{-3} in 2.8 mm diameter) that radiates the bulk of the K-shell power, and a much cooler (110eV, 2.5×10^{19} cm^{-3} in $\Delta r = 2.6$ mm) outer blanket bearing 73% of the total mass.

Figure 5-5 shows radial line-outs of the simulated density at four times during stagnation, still in the QN treatment. The on-axis magnitudes are three orders of magnitude larger than the data suggest, but this is typical of 2D models.

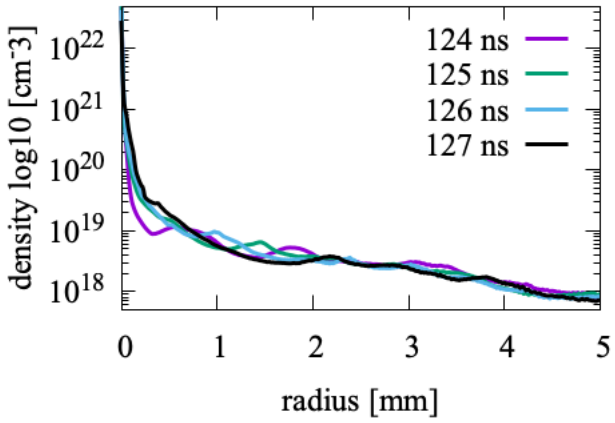

Figure 5-5 Radial line-outs of the Ar ion density during stagnation in 2D QN.

The rough initial analysis does not *invalidate* the CHICAGO model, but more density/temperature analysis is needed. Additionally, a crude simulation-to-data comparison of the x-ray radiation output is supplied in Table 5-1. The 2D yields are higher than data, which is common. The radiation transport in CHICAGO solves the diffusion equation, which is not uncommon but not the more accurate non-LTE solution. It is not clear if the simulation suffers from a poorly vetted EOS, but we note that the state tables are from the 1980's and likely much older than those used in recent MHD models in Refs. [18], [29], and [25]. The time to implosion (t_{impl}) would be more accurately captured in the simulation and does agree with data. The definition of t_{impl} used for the simulation is the time between the rise in current to first bounce.

Table 5-1 Total x-ray output from Ar gas-puff experiments on Z and 2D simulation. The measurements are reproduced from Ref. [19]

shot	yield [kJ]	power [TW]	t_{impl} [ns]
2559	816 ± 20%	41.4	104.2
2560	1005 ± 20%	40.3	102.9
2561	905 ± 20%	44.6	103.6
simulation	1177	53.6	104.2

The results for the hybrid technique, in which a transition to kinetic is performed at 103.6 ns, is plotted in Fig. 5-6. The density distributions are preserved, as well as total charge, shown during

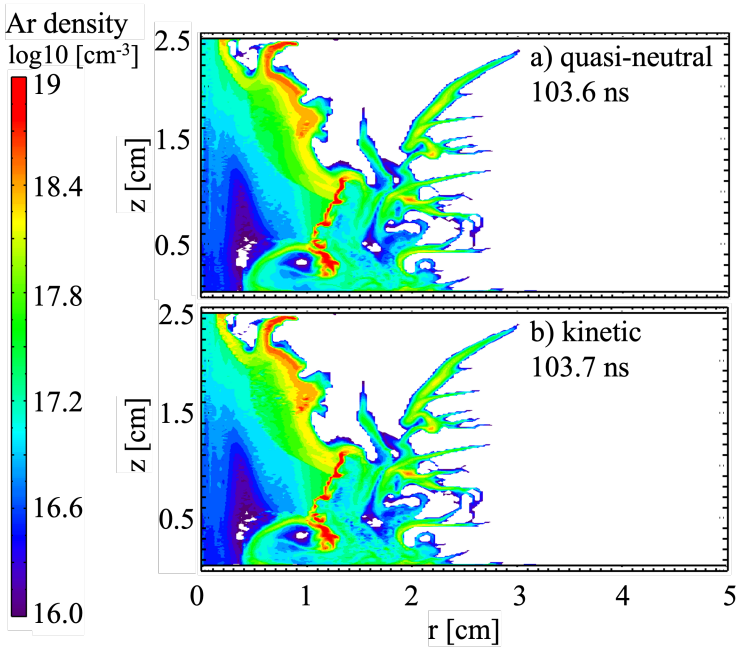

Figure 5-6 The Ar ion density distributions across the hybrid transition. The QN density is shown in a) at 103.6 ns and the kinetic particles are shown in b) at 103.7 ns.

migration in Fig. 5-7a. However, energy is poorly conserved, as shown in Fig. 5-7b. The number of kinetic particles specified is 120 electrons and 50 ions for every QN particle, which was sufficient in 1D. The 1D model uses 5 μm grid cells while the 2D uses 10 μm, and this likely has an impact. We estimate that the high-density regions in Fig. 5-6 likely require hundreds of kinetic particles per QN ion. This is being investigated.

For completeness, the kinetic electron energy distribution immediately after transition is plotted in Fig. 5-8. Given the poor energy conservation in Fig. 5-7b, subsequent energy distributions would suffer numerical cooling.

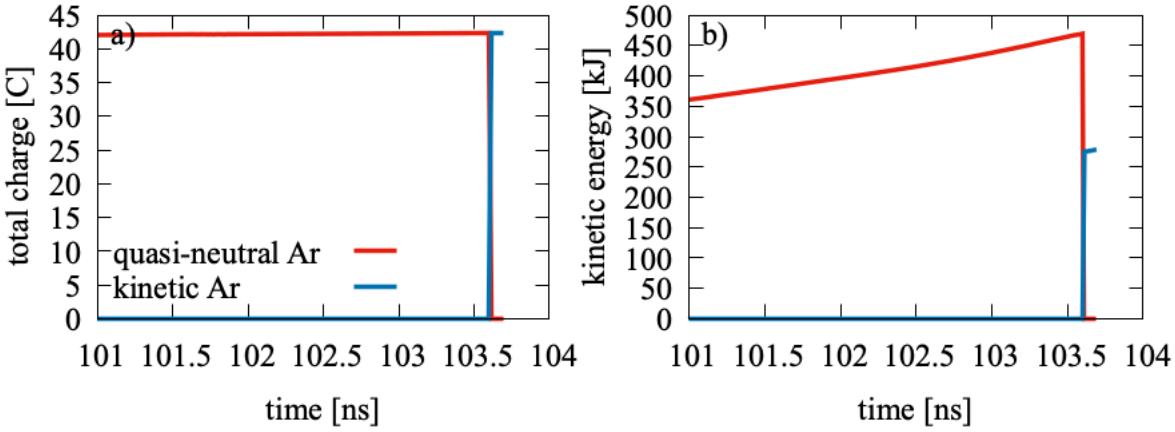

Figure 5-7 The summed Ar ion a) charge and b) kinetic energy in the 2D gas puff simulation with a QN to kinetic migration at 103.6 ns.

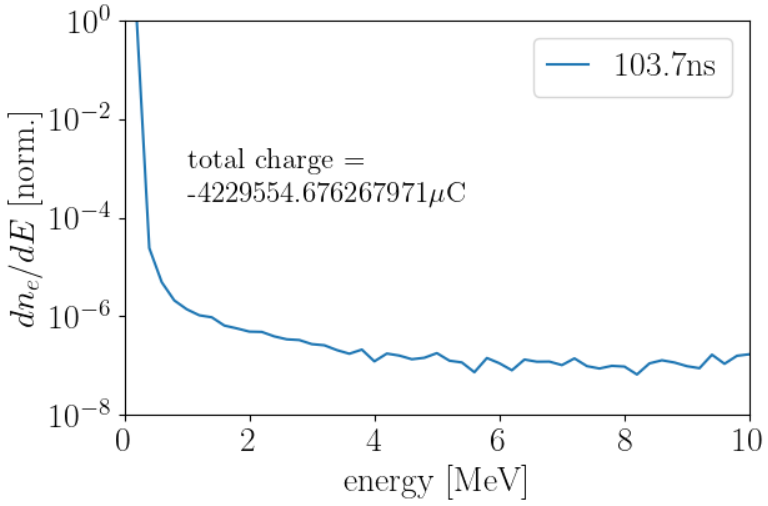

Figure 5-8 The electron energy distribution at 103.7 ns in a hybrid 2D Ar gas puff with a transition at 103.6 ns.

6. WIRE ARRAY DYNAMICS

A 2D cylindrical (r, z) molybdenum (Mo) wire array simulation is designed for comparison to Z shot z2533 that features in Ref. [3]. The configuration is a nested wire array of pure Mo. The outer array has a 2.5-cm radius and the inner array has a 1.25-cm radius with a total mass of 2.68 mg.

To model the inherent 3D structure of a wire array in 2D, the wires are initialized as partially ablated, forming two uniform annuli. These less-than-solid-density wires have the correct mass but span $\Delta r = 1$ mm. With the simulation resolution of 20 μm, the initial Mo density distributions, illustrated Fig. 6-1a, span 50 cells. Driven by a realistic Z pulse, the wires reach stagnation at 129 ns (3079 ns machine time). This is consistent with the pulse shapes in Fig. 1 of Ref. [17]. The Mo density distributions are shown at six times during implosion in Fig. 6-1. (As with the 2D Ar gas-puff model in Fig. 5-4, it is not clear if the plasma behavior at the interface with the perfectly conducting boundaries is realistic.)

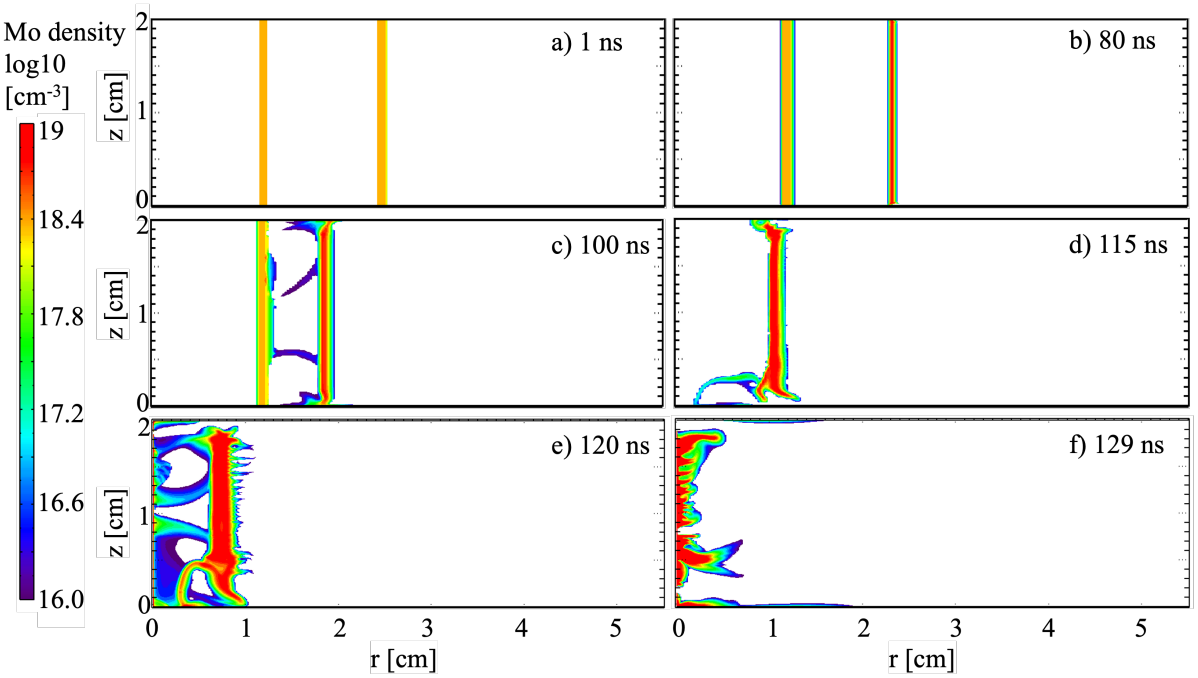

Figure 6-1 The Mo wire-array implosion in a 2D QN simulation. The Mo density distributions are shown at six times: a) 1, b) 80, c) 100, d) 115, e) 120, and f) 129 ns.

The simulated radiation pulse begins to rise at the same time as the data in Fig. 1 of Ref. [17], but the yield calculated using a "cold" opacity table is, at 20 kJ, two orders of magnitude too high. The discrepancy could be due to any combination of outstanding issues unrelated to the code algorithms. For example, work must continue to ensure the EOS and opacity values are being calculated properly. The CHICAGO-generated $\bar{Z}$ and electron temperatures are well below the average values of $\bar{Z} = 33.7$ and $T_e \approx 4$ keV predicted in the SCRAM model. In addition, the radiation transport feedback to the plasma became numerically unstable at 115 ns (just after the output Fig. 6-1d.) It is also likely that some amount of mass must is lost during the ablation phase,

with as much as 95% predicted in Ref. [17]. A 3D model would capture asymmetries that decrease the yield, as seen in the spatially resolved spectra in Fig. 1 of Ref. [17].

7. CONCLUSION

We described a new hybrid code capability that is better suited to predict and optimize non-thermal yield. Studies on the Z Machine have shown that non-thermal sources have similar implosion characteristics but different pinch stagnation profiles from thermal sources [1]. To capture both stages as accurately as possible, a hybrid particle treatment has been implemented in the fully-relativistic electromagnetic PIC code CHICAGO [34, 8, 5, 32, 22]. The ionization and implosion stages are modeled with a fast, QN particle treatment, similar to an MHD fluid in which electrons are not tracked but assumed to follow the ions. This includes the assumption of local thermal equilibrium with an EOS and radiation transport. Prior to stagnation, the particles are transitioned to fully-kinetic electrons and ions. Tracking electrons requires high spatial, temporal, and charge resolution, as demonstrated in Ref. [7], but provides the more accurate, discrete particle energy distributions that drive non-thermal processes. The field and particle space-charge dynamics are calculated self-consistently. At present, the non-LTE spectral features are calculated in a post-processing step. While the thermal, LTE spectrum is modeled in the QN phase, a self-contained calculation of the non-thermal particle generation and output photon spectrum requires considerable further development.

The resolution requirements for this code capability were determined in simulations of an idealized 1D Ar gas puff. Separately testing all three available particle treatments, without transitions, we determined that there are no benefits to using multi-fluid particles in a load model. The multi-fluid particles had the idealized sheath behavior of a QN particle with the resolution requirements of kinetic electrons. The result was an ever-tightening sheath, with increasing number density. This required ever-smaller time steps to comply with limits on $\omega_{ce}\Delta t$ and $\omega_p\Delta t$.

Some very preliminary code validation was performed using a 2D Ar gas puff and a 2D Mo wire array. The simulated x-ray yield for the Ar gas puff is within 25% of measurements and the implosion times agree within a few percent. The implosion trajectory of a Mo wire array is also reproduced in the CHICAGO model, however a new EOS and opacity table is needed.

Both of these exemplar represents the type of non-thermal source simulation that will utilize the hybrid code capability going forward. The code will be used for non-thermal source development as well as for understanding the non-thermal effects measured in thermal z-pinch sources.

This page intentionally left blank.

REFERENCES

[1] D. J. Ampleford, S. B. Hansen, C. A. Jennings, B. Jones, C. A. Coverdale, A. J. Harvey-Thompson, G. A. Rochau, G. Dunham, N. W. Moore, E. C. Harding, M. E. Cuneo, Y.-K. Chong, R. W. Clark, N. Ouart, J. W. Thornhill, J. Giuliani, and J. P. Apruzese. Opacity and gradients in aluminum wire array z-pinch implosions on the Z pulsed power facility. *Phys. Plasmas*, 21(3):031201, 2014.

[2] D. J. Ampleford, C. A. Jennings, B. Jones, S. B. Hansen, M. E. Cuneo, C. A. Coverdale, M. C. Jones, T. M. Flanagan, M. Savage, W. A. Stygar, M. R. Lopez, J. P. Apruzese, J. W. Thornhill, J. L. Giuliani, and Y. Maron. K-shell emission trends from 60 to 130 cm/μs stainless steel implosions. *Phys. Plasmas*, 20(10):103116, 2013.

[3] David J. Ampleford, Stephanie B Hansen, Christopher A Jennings, Timothy J. Webb, Victor Harper-Slaboszewicz, Guillaume P. Loisel, Timothy M. Flanagan, Kate S. Bell, Brent Jones, Leroy A. McPherson, Gregory A. Rochau, Jeremy P. Chittenden, Mark Sherlock, Brian Appelbe, John Giuliani, Nicholas Ouart, and John Seely. Non-thermal x-ray emission from wire array z-pinches. Technical Report SAND2015-10453, Sandia National Laboratories, 2015.

[4] R. Balescu. *Transport Processes in Plasmas*. North Holland, Amsterdam, 1988.

[5] N. Bennett, M. Blasco, K. Breeding, D. Constantino, A. DeYoung, V. DiPuccio, J. Friedman, B. Gall, S. Gardner, J. Gatling, E. C. Hagen, A. Luttman, B. T. Meehan, M. Misch, S. Molnar, G. Morgan, R. O'Brien, L. Robbins, R. Rundberg, N. Sipe, D. R. Welch, and V. Yuan. Development of the dense plasma focus for short-pulse applications. *Phys. Plasmas*, 24(1):012702, 2017.

[6] N. Bennett, D. R. Welch, C. A. Jennings, E. Yu, M. H. Hess, B. T. Hutsel, G. Laity, J. K. Moore, D. V. Rose, K. Peterson, and M. E. Cuneo. Current transport and loss mechanisms in the z accelerator. *Phys. Rev. Accel. Beams*, 22:120401, Dec 2019.

[7] N. Bennett and D.R. Welch. Resolution requirements for energy conservation in kinetic plasma simulations. Technical Report SAND2022-13998, Sandia National Laboratories, 2022.

[8] Nichelle Bennett, Dale R. Welch, Timothy J. Webb, Michael G. Mazarakis, Mark L. Kiefer, M. Dale Crain, Darryl W. Droemer, Raymond E. Gignac, Mark D. Johnston, Joshua J. Leckbee, Isidro Molina, Dan Nielsen, Robert Obregon, Tobias Romero, Sean Simpson, Chase C. Smith, Frank L. Wilkins, and Derek Ziska. The impact of plasma dynamics on the self-magnetic-pinch diode impedance. *Phys. Plasmas*, 22(3):033113, 2015.

[9] C. K. Birdsall and A. B. Langdon. *Plasma Physics via Computer Simulation*. Adam Hilger, New York, 1991.

[10] T.J.M. Boyd and J.J. Sanderson. *The Physics of Plasmas*. Cambridge University Press, 2003.

[11] S. I. Braginskii. Transport Processes in a Plasma. In M. A. Leontovich, editor, *Reviews of Plasma Physics*, volume 1, page 205. Consultants Bureau, New York, 1965.

[12] C.A. Coverdale, K.S. Bell, T.M. Flanagan, N. W. Moore, V. Harper-Slaboszewicz, B. Ulmen, D.J. Ampleford, L.A. McPherson, G. Loisel, and G. Laity. Warm x-ray platform work on the z machine: Radiation effects test objects and diagnostic development. Technical Report SAND2017-1396, Sandia National Laboratories, 2017.

[13] C.A. Coverdale, B. Jones, D.J. Ampleford, J. Chittenden, C. Jennings, J.W. Thornhill, J.P. Apruzese, R.W. Clark, K.G. Whitney, A. Dasgupta, J. Davis, J. Guiliani, P.D. LePell, C. Deeney, D.B. Sinars, and M.E. Cuneo. K-shell x-ray sources at the Z accelerator. *High Energy Density Physics*, 6(2):143–152, 2010. ICHED 2009 - 2nd International Conference on High Energy Density Physics.

[14] M. E. Cuneo, D. B. Sinars, E. M. Waisman, D. E. Bliss, W. A. Stygar, R. A. Vesey, R. W. Lemke, I. C. Smith, P. K. Rambo, J. L. Porter, G. A. Chandler, T. J. Nash, M. G. Mazarakis, R. G. Adams, E. P. Yu, K. W. Struve, T. A. Mehlhorn, S. V. Lebedev, J. P. Chittenden, and C. A. Jennings. Compact single and nested tungsten-wire-array dynamics at 14–19MA and applications to inertial confinement fusion. *Phys. Plasmas*, 13(5):056318, 2006.

[15] B. Jones *et al.* Advanced K-shell radiation sources for radiation effects sciences on Z. Technical Report SAND2012-8150, Sandia National Laboratories, 2012.

[16] T. C. Genoni, R. E. Clark, and D. R. Welch. A fast implicit algorithm for highly magnetized charged particle motion. *The Open Plasma Physics Journal*, 3:36, 2010.

[17] S. B. Hansen, D. J. Ampleford, M. E. Cuneo, N. Ouart, B. Jones, C. A. Jennings, A. Dasgupta, C. A. Coverdale, G. A. Rochau, G. Dunham, J. L. Giuliani, and J. P. Apruzese. Signatures of hot electrons and fluorescence in Mo Kα emission on Z. *Phys. Plasmas*, 21(3):031202, 2014.

[18] A. J. Harvey-Thompson, C. A. Jennings, B. Jones, J. P. Apruzese, D. J. Ampleford, D. C. Lamppa, C. A. Coverdale, M. E. Cuneo, J. L. Giuliani, S. B. Hansen, M. C. Jones, N. W. Moore, G. A. Rochau, and J. W. Thornhill. Investigating the effect of adding an on-axis jet to Ar gas puff z pinches on Z. *Phys. Plasmas*, 23(10):101203, 2016.

[19] B. Jones, J. P. Apruzese, A. J. Harvey-Thompson, D. J. Ampleford, C. A. Jennings, S. B. Hansen, N. W. Moore, D. C. Lamppa, D. Johnson, M. C. Jones, E. M. Waisman, C. A. Coverdale, M. E. Cuneo, G. A. Rochau, J. L. Giuliani, J. W. Thornhill, N. D. Ouart, Y. K. Chong, A. L. Velikovich, A. Dasgupta, M. Krishnan, and P. L. Coleman. The effect of gradients at stagnation on K-shell x-ray line emission in high-current Ar gas-puff implosions. *Phys. Plasmas*, 22(2):020706, 02 2015.

[20] Brent Jones, Christine A. Coverdale, Christopher Deeney, Daniel B. Sinars, Eduardo M. Waisman, Michael E. Cuneo, David J. Ampleford, P. David LePell, Kyle R. Cochrane, J. Ward Thornhill, J. P. Apruzese, Arati Dasgupta, Kenneth G. Whitney, Robert W. Clark, and Jeremy P. Chittenden. Implosion dynamics and K-shell x-ray generation in large diameter stainless steel wire array z pinches with various nesting configurations. *Phys. Plasmas*, 15(12):122703, 2008.

[21] Brent Jones, Christopher A. Jennings, Derek C. Lamppa, Stephanie B. Hansen, Adam J. Harvey-Thompson, David J. Ampleford, Michael E. Cuneo, Thomas Strizic, Drew Johnson, Michael C. Jones, Nathan W. Moore, Timothy M. Flanagan, John L. McKenney, Eduardo M. Waisman, Christine A. Coverdale, Mahadevan Krishnan, Philip L. Coleman, Kristi Wilson Elliott, Robert E. Madden, John Thompson, Alex Bixler, J. Ward Thornhill, John L. Giuliani, Young K. Chong, Alexander L. Velikovich, Arati Dasgupta, and John P. Apruzese. A renewed capability for gas puff science on Sandia's Z Machine. *IEEE Trans. Plasma Sci.*, 42(5):1145–1152, 2014.

[22] George R. Laity, Allen C. Robinson, Michael E. Cuneo, M. Kathleen Alam, Kristian R. C. Beckwith, Nichelle L. Bennett, Matthew T. Bettencourt, Stephen D. Bond, Kyle Cochrane, Louise Criscenti, Eric C. Cyr, Karen De Zetter, Richard R. Drake, Evstati G. Evstatiev, Andrew S. Fierro, Thomas A. Gardiner, Forrest W. Glinesa, Ronald S. Goeke, Nathaniel D. Hamlin, Russell Hooper, Jason Koski, J. Matthew Lane, Steven R. Larson, Kevin Leung, Duncan A. McGregor, Philip R. Miller, Sean M. Miller, Susan J. Ossareh, Edward G. Phillips, Nicholas A. Roberds, Charles E. Rose, John N. Shadid, Sidney Shields, Sean C. Simpson, David Sirajuddina, Thomas M. Smith, M. Scot Swan, Aidan P. Thompson, and Julien G. Tranchida. Towards predictive plasma science and engineering through revolutionary multi-scale algorithms and models, final report. Technical Report SAND2021-0718, Sandia National Laboratories, 2021.

[23] P. W. Rambo and R. J. Procassini. A comparison of kinetic and multifluid simulations of laser-produced colliding plasmas. *Phys. Plasmas*, 2(8):3130–3145, 1995.

[24] H. Sze, P. L. Coleman, J. Banister, B. H. Failor, A. Fisher, J. S. Levine, Y. Song, E. M. Waisman, J. P. Apruzese, R. W. Clark, J. Davis, D. Mosher, J. W. Thornhill, A. L. Velikovich, B. V. Weber, C. A. Coverdale, C. Deeney, T. L. Gilliland, J. McGurn, R. B. Spielman, K. W. Struve, W. A. Stygar, and D. Bell. Efficient argon K-shell radiation from a Z pinch at currents >15 MA. *Phys. Plasmas*, 8(7):3135–3138, 2001.

[25] V. Tangri, A. J. Harvey-Thompson, J. L. Giuliani, J. W. Thornhill, A. L. Velikovich, J. P. Apruzese, N. D. Ouart, A. Dasgupta, B. Jones, and C. A. Jennings. Simulations of Ar gas-puff Z-pinch radiation sources with double shells and central jets on the Z generator. *Phys. Plasmas*, 23(10), 10 2016.

[26] C. Thoma, D. R. Welch, R. E. Clark, N. Bruner, J. J. MacFarlane, and I. E. Golovkin. Two-fluid electromagnetic simulations of plasma-jet acceleration with detailed equation-of-state. *Phys. Plasmas*, 18(10):103507, 2011.

[27] C. Thoma, D. R. Welch, R. E. Clark, D. V. Rose, and I. E. Golovkin. Hybrid-pic modeling of laser-plasma interactions and hot electron generation in gold hohlraum walls. *Phys. Plasmas*, 24(6):062707, 2017.

[28] C. Thoma, D.R. Welch, and D.V. Rose. Implicit highly-coupled single-ion hall-mhd formulation for hybrid particle-in-cell codes. *Comp. Phys. Comm.*, 261:107823, 2021.

[29] J. Ward Thornhill, John L. Giuliani, Brent Jones, John P. Apruzese, Arati Dasgupta, Young K. Chong, Adam J. Harvey-Thompson, David J. Ampleford, Stephanie B. Hansen, Christine A. Coverdale, Christopher A. Jennings, Gregory A. Rochau, Michael E. Cuneo,

Derek C. Lamppa, Drew Johnson, Michael C. Jones, Nathan W. Moore, Eduardo M. Waisman, Mahadevan Krishnan, and Philip L. Coleman. 2-D RMHD modeling assessment of current flow, plasma conditions, and doppler effects in recent z argon experiments. *IEEE Trans. Plasma Sci.*, 43(8):2480–2491, 2015.

[30] R. Vesey, S. Hansen, and P.J. Christenson. Design and testing of warm x-ray and fast neutron sources on z to support the hostile environments gc-ldrd. Technical Report SAND2016-9852, Sandia National Laboratories, 2016.

[31] D. R. Welch, N. Bennett, T. C. Genoni, D. V. Rose, C. Thoma, C. Miller, and W. A. Stygar. Electrode contaminant plasma effects in 10^7-ampere z pinch accelerators. *Phys. Rev. Accel. Beams*, 22:070401, 2019.

[32] D. R. Welch, N. Bennett, T. C. Genoni, C. Thoma, and D. V. Rose. Fast hybrid particle-in-cell technique for pulsed-power accelerators. *Phys. Rev. Accel. Beams*, 23:110401, Nov 2020.

[33] D. R. Welch, D. V. Rose, B. V. Oliver, E. Schamiloglu, K. Hahn, and J. E. Maenchen. Transport of a relativistic electron beam in gas and plasma-filled focusing cells for x-ray radiography. *Phys. Plasmas*, 11(2):751–760, 2004.

[34] Dale R. Welch, David V. Rose, Nichelle Bruner, Robert E. Clark, Bryan V. Oliver, Kelly D. Hahn, and Mark D. Johnston. Hybrid simulation of electrode plasmas in high-power diodes. *Phys. Plasmas*, 16(12):123102, 2009.

DISTRIBUTION

Email—Internal

Name	Org.	Sandia Email Address
Brent Jones	1381	bmjones@sandia.gov
Luke Shulenburger	1684	lshulen@sandia.gov
Nichelle Bennett	1684	nlbenne@sandia.gov
Technical Library	1911	sanddocs@sandia.gov

Email—External

Name	Company Email Address	Company Name
Dale Welch	dale.welch@vosssci.com	Voss Scientific. LLC

Hardcopy—Internal

Number of Copies	Name	Org.	Mailstop
1	L. Martin, LDRD Office	1910	0359

Sandia National Laboratories is a multimission laboratory managed and operated by National Technology & Engineering Solutions of Sandia LLC, a wholly owned subsidiary of Honeywell International Inc., for the U.S. Department of Energy's National Nuclear Security Administration under contract DE-NA0003525.